Nanoscale assembly of silicon-like $[Al(As_{1-x}N_x)]_ySi_{5-2y}$ alloys: Fundamental theoretical and experimental studies of structural and optical properties

L. Jiang,[1] P. E. Sims,[2] G. Grzybowski,[2] R. T. Beeler,[2] A. V. G. Chizmeshya,[2] D. J. Smith,[1] J. Kouvetakis,[2] and J. Menéndez[1]

[1]*Department of Physics, Arizona State University, Tempe, Arizona 85287-1504, USA*

[2]*Department of Chemistry and Biochemistry, Arizona State University, Tempe, Arizona 85287-1604, USA*

(Received 25 January 2013; published 31 July 2013)

Ab initio theoretical simulations of $Al(As_{1-x}N_x)Si_3$ alloys, a new class of optoelectronic materials, confirm that these compounds are likely to be disordered via a mechanism that preserves the integrity of the constituent III-V-Si_3 tetrahedra but randomizes their orientation in the average diamond lattice of the compound. This type of disorder is consistent with experimental structural data and with the proposed growth mechanism for such alloys, according to which "III:V$(SiH_3)_3$" intermediate complexes are formed in the gas phase from reactions between group-III atomic beams and $V(SiH_3)_3$ molecules, delivering the entire III-V-Si_3 tetrahedra to the growing film. Experimental optical studies of these $Al(As_{1-x}N_x)Si_3$ alloys as well as more general $[Al(As_{1-x}N_x)]_ySi_{5-2y}$ compounds grown on Si substrates were carried out using spectroscopic ellipsometry. The resulting dielectric functions are found to be similar to broadened versions of their counterparts in pure Si. This broadening may have important practical applications, particularly in photovoltaics, because it dramatically enhances the optical absorption of Si in the visible range of the electromagnetic spectrum. A critical point analysis reveals the existence of direct optical transitions at energies as low as 2.5 eV, well below the lowest direct absorption edge of Si at 3.3 eV. Such transitions are predicted theoretically for perfectly ordered III-V-Si_3 compounds, and the experimental results suggest that they are robust against tetrahedra orientational disorder.

DOI: 10.1103/PhysRevB.88.045208 PACS number(s): 78.40.Fy, 61.66.Dk, 61.72.uf, 61.72.uj

I. INTRODUCTION

The frustration of the zincblende ordering in alloys of III-V and group-IV semiconductors is of fundamental interest in semiconductor physics.[1–8] (III-V)-IV alloys are also attractive from the point of view of applications such as photovoltaics, which calls for semiconductors with identical lattice parameters and different band gaps to form multijunction solar cells. III-V compounds and group-IV materials from the same row of the periodic table meet this criterion, and one might expect their alloys to offer tunable band gaps that can be exactly matched to photovoltaic requirements. In fact, the $(GaAs)_{1-x}Ge_{2x}$ alloy has been proposed as a system lattice-matched to Ge with a 1 eV band gap for $x \simeq 0.1$ (Ref. 9), as needed to increase the efficiency of Ge-InGaAs-GaAsP solar cells by inserting an additional junction between the Ge and InGaAs subcells.[10,11] Unfortunately, this intriguing technological potential has not been realized until now due to the severe phase separation issues that plague these systems.

The growth of (III-V)-IV alloys has usually been carried out using techniques such as molecular beam epitaxy (MBE), metal-organic chemical vapor deposition, or sputtering, which deliver individual atomic species separately.[9,10,12–14] Theoretical simulations of the growth mechanism have also been based on this assumption.[3,4] An alternative approach was recently introduced by our group.[15] We reasoned that the risk of phase separation could be minimized by using growth precursor molecules that incorporate at least one of the IV-III or IV-V bonds desired in the solid phase. For the first practical realization of this approach, we combined $P(SiH_3)_3$ molecules with atomic Al beams from a Knudsen cell to grow the $AlPSi_3$ compound on Si substrates in a gas-source MBE reactor. Structural studies of the films showed pseudomorphic growth with excellent crystallinity and no indication of phase separation.[15] The method was later extended to nonstoichiometric $(AlP)_xSi_{5-2x}$ alloys[16] as well as to other group-V elements such as N and As.[17,18] In all cases, we find that the group-III and group-V elements are incorporated in a 1:1 ratio within experimental error, and that the lattice parameter of the resulting alloys approach the Vegard average between Si and the corresponding III-V compound. These findings suggest that the growth proceeds via the formation of "Al:P$(SiH_3)_3$" intermediates whose tetrahedral (Al-P)-Si_3 cores are directly incorporated into the growing diamondlike solid.

The availability of entirely new families of Si-compatible compounds creates opportunities in the field of Si photovoltaics. While crystalline Si dominates the solar cell market, its properties are far from ideal for photovoltaic applications. The lowest direct band gap of Si has an energy of 3.3 eV (Ref. 19), so that most of the photons in Si solar cells are absorbed via inefficient indirect transitions that require thick layers and expensive light-trapping mechanisms. The incorporation of III-V elements into Si has been recently proposed as a way to enhance the absorption by direct optical transitions.[20] Our method accomplishes this goal using an elegant approach that reaches the maximum possible concentration of isolated "donor-acceptor" pairs within fully interlinked III-V-$(IV)_3$ building blocks (see Fig. 1) in a diamond-structure matrix. On the other hand, to the extent that the lowest band gap of our (III-V)-IV alloys is higher than that of Si, the new materials may represent an alternative to GaNPAs (Ref. 21) or metamaterials[22] for Si-based dual-junction solar cells. Recent theoretical simulations confirm that $AlPSi_3$ as well as $AlAsSi_3$ are indeed expected to have fundamental indirect band gaps higher than the Si band gap of 1.1 eV.[17,23] Moreover, the calculations show that $AlPSi_3$ and $AlAsSi_3$ have increased absorption in the visible area due in part to the existence of direct optical transitions at energies below those of the

 ©2013 American Physical Society

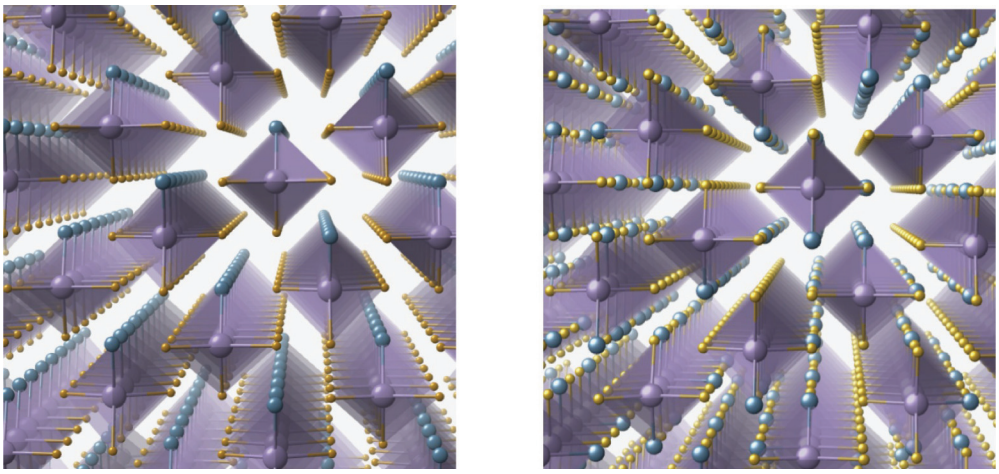

FIG. 1. (Color online) Structural models of the $AlAsSi_3$-ordered ground state (left) and the orientationally disordered analog (right) in which both structures share a common As-atom sublattice and are both devoid of Al-Al bonds. The orientational disorder of the Al-As bonds is reflected in the random distribution of the Al atoms (medium-size spheres). Si (As) atoms are shown as small (large) spheres, and the $AlAsSi_3$ units are shown as tetrahedra.

corresponding transitions in Si. This energy lowering deviates from an interpolation between Si and the corresponding III-V compound due to level repulsion caused by the lower symmetry of the III-V-Si_3 materials.

The theoretical calculations were performed on the lowest energy arrangements of Al-V-Si_3 tetrahedra, which yield ordered crystals with as little as 10 atoms per unit cell. However, it is far from obvious that such structures can be realized in practice. In fact, Raman spectra from different Al-V-Si_3 materials do not exhibit the several sharp lines expected from perfect crystals with 10–20 atoms per unit cell, but they rather show broadened features as seen in other semiconductor alloys.[17] This observation raises two important issues. First, the lack of vibrational spectroscopy evidence for the lowest energy tetrahedral arrangements could be interpreted as an indication that the proposed growth mechanism via Al-V-Si_3 tetrahedra is an oversimplification. Second, the predicted low energy direct optical transitions may not be observable in real systems, since they were computed for crystals with small unit cells. In this paper, we present a combined theoretical and experimental study to address these issues. We show that crystals in which the structural Al-V-Si_3 tetrahedra are preserved but their orientations are randomized (as seen in Fig. 1, right), while avoiding direct Al-Al bonds, have energies only marginally higher than the ground state structures. These orientationally disordered structures, which are highly likely to be formed, are consistent with the proposed growth mechanism via Al-V-Si_3 tetrahedra and may offer a natural explanation for the broadened Raman spectra. On the other hand, we determined the dielectric function of several samples using spectroscopic ellipsometry, and we find that the low energy direct transitions predicted by theoretical studies can indeed be observed, suggesting that these transitions are robust against orientational disorder and may in fact be enhanced.

The experimental studies were carried out on $[Al(As_{1-x}N_x)]_ySi_{5-2y}$ films. The choice of this material system is dictated by both practical and theoretical considerations. First, as we indicated in prior work,[18] the presence of nitrogen is necessary to achieve perfect lattice matching to Si, which is an important requirement for photovoltaic applications. On the other hand, nitrogen may both increase the energy of the indirect gap due to the very large band gaps of cubic AlN, while at the same time lowering the energy of direct optical transitions if giant bowing effects such as those seen in $GaAs_{1-x}N_x$ alloys are also present in $[Al(As_{1-x}N_x)]_ySi_{5-2y}$. The use of P instead of As would facilitate lattice-matching with Si and may eventually become the best choice for applications, but the mass and atomic number similarity with Si make microscopy and spectroscopic characterization more challenging. Finally, the use of alloys with varying y values introduces an additional degree of freedom that may provide some insight into disordering effects in Al-V-Si_3 materials. In particular, since the additional Si atoms in structures with $y < 1$ are presumably incorporated at random sites, the Al-As-Si_3 and Al-N-Si_3 tetrahedra in these materials will necessarily be oriented at random, while alloys such as $Al(As_{1-x}N_x)Si_3$ could in principle possess full orientational order.

The paper in organized as follows. In Sec. II, we present our theoretical analysis of orientational tetrahedral disorder. In Sec. III, we describe the synthesis and structural characterization of $[Al(As_{1-x}N_x)]_ySi_{5-2y}$ films, and in Sec. IV, we present and discuss our spectroscopic ellipsometry measurements of the dielectric function of these materials.

II. THEORETICAL SIMULATIONS OF ALLOY DISORDER

Our initial structural interpretation of Al-(V)-Si_3 systems was based on high-symmetry crystalline models with ordered 10-atom and 20-atom representations of the ground state structures based on the diamond-cubic lattice.[15–18] The lowest energy configurations were identified as *C1c1* symmetry structures in which thermodynamically unfavorable Al-Al bonds were precluded by design with a common orientation for all III-V pairs. Our proposed ordered models allowed electronic structure and vibrational studies to be efficiently

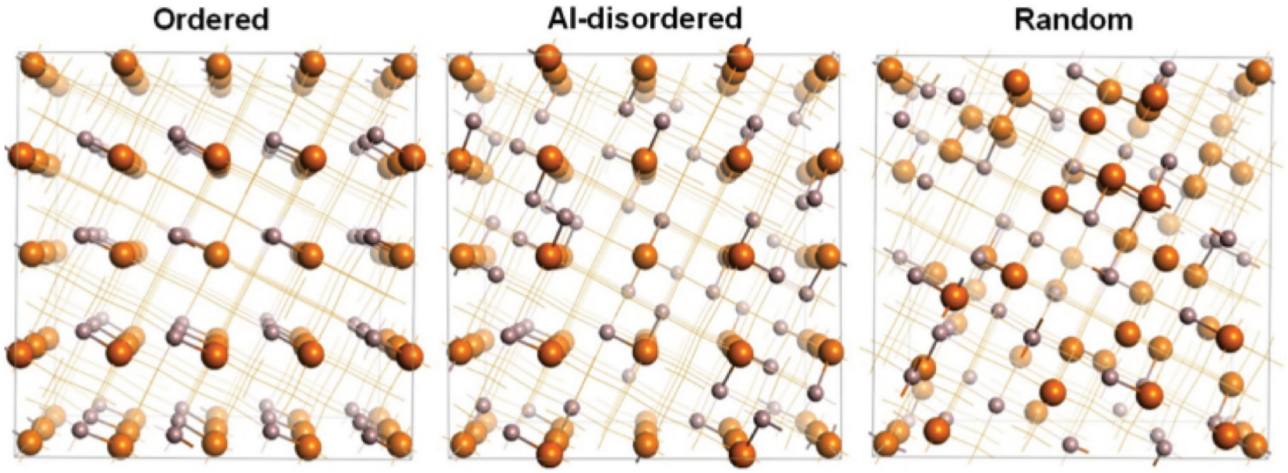

FIG. 2. (Color online) Structurally optimized 240-atom supercell models of the $AlAsSi_3$ system corresponding to completely ordered *C1c1* ground state (top left), a state in which the Al-As-Si_3 units are rotationally disordered (by exchanging Al and Si atoms about each As atom) while avoiding Al-Al bonds (top center) and a conventional alloy model in which the Al, As, and Si constituents are randomly distributed on silicon lattice sites (top right). Aluminum and arsenic atoms are shown as grey and orange spheres, respectively, and the silicon sublattice is drawn using faint gold lines to emphasize the III-V site configurations.

carried out,[17,18] and preliminary comparisons were to be made with experiment. While the energy penalty associated with Al-Al bonding is significant, a myriad of energetically similar ordered structures can be formed involving short-range orientational motifs among neighboring III-V-IV_3 units. An example is shown in Fig. 2 of Ref. 15 for the $AlPSi_3$ system, where these higher energy configurations are typically 10–20 meV/atom above the energy of the ordered ground state. In this study, we pursue a series of larger scale calculations of disordered structures in order to compare their energetic stability and structural properties with those of their ordered counterparts. The concept of orientational disorder of III-V bonds was used to rationalize both the electronic and vibrational behavior in our previous work on the $Al(As_{1-x}P_x)Si_3$ analogs.[17] In the latter case, the data suggested that alloy disorder is responsible for the observation of Raman peaks that are asymmetrically broadened with respect to pure Si.

As a starting point we first considered the $AlAsSi_3$ system and then extended our treatment to the $Al(As_{0.9}N_{0.1})Si_3$ alloy derivative as one of the target systems in the experimental part of this study. Beginning with a 20-atom representation[17] we constructed $2 \times 2 \times 3$ supercells containing 240 atoms, or 48 (III-V)IV_3 building units. To generate a pseudorandom orientational distribution of Al-As bonds on a Si lattice, consistent with the incorporation of complete Al-As-Si_3 building blocks, we first constructed a Si_4As crystal by arranging the As atoms on a regular third-nearest-neighbor sublattice following a chess knight's move motif, as described in our initial studies.[15] At each As site, one of the four Si atom neighbors is replaced by an Al atom and then tested for a neighboring Al atom to avoid the creation of an Al-Al bond. A random walk is then performed throughout the lattice on the remaining As sites using this procedure until all sites are exhausted, and a configuration with no Al-Al bonds and randomly oriented Al-As bonds is generated. A representative configuration, denoted as Al-disordered, is shown in Fig. 2, where it is compared to the corresponding perfectly ordered *C1c1* symmetry ground state. A completely random III-V-IV_3 alloy model, which disregards the existence of III-V-IV_3 building units, is also shown for comparison. Using essentially the same strategy, we then calculated the corresponding properties of $Al(As_{0.9}N_{0.1})Si_3$. In this case, five N atoms were randomly distributed on the 48 available As sublattice sites within the 240-atom supercell.

In all cases, the simulations were carried out using a density functional theory (DFT) framework, as implemented in the Vienna *Ab initio* Simulation Package (VASP) code[24–26] within the well-known local density approximation (LDA).[27] Comparing generalized gradient approximation (GGA) and LDA simulations on similar III-V-IV systems, we find that energy differences, the primary objective of our simulations, are very insensitive to the choice of exchange-correlation functional. As far as the structural predictions are concerned, the LDA slightly underestimates length scales while the GGA yields overestimated values. We used the so-called ultrasoft pseudopotentials to replace the core electrons by an effective potential acting on the valence electrons. Electronic states were expanded in a plane wave basis with an overall energy cutoff of 400 eV using a single k-point centered at Γ for Brillouin zone sampling. Using these computational conditions, the supercell shape, dimensions, and all atomic positions were optimized to yield accurate equilibrium structures with a residual cell stress and atomic forces of less than ∼0.01 kbar and ∼0.005 eV/Å, respectively.

The equilibrium structural parameters, also shown in Table I, indicate that the lattice parameters of the ordered and orientationally disordered configurations are virtually identical for $AlAsSi_3$. This is the expected outcome, since the only distinction between the latter two systems is the distribution of Al atoms about the As sites, which themselves form an ordered sublattice in both cases. The first-nearest neighbor (1NN) bond distributions in these two systems are thus identical by definition, apart from minute bond-length variations induced by differences at the second-nearest neighbor (2NN) level.

TABLE I. Cell parameters and energies for the three types of model structures depicted in Fig. 2. Notice that in this crystallographic setting the ideal c/a ratio for the diamond lattice is $\sqrt{9/10} \sim 0.949$.

	Lattice parameters								ΔE	ΔG
Model	a(Å)	b(Å)	c(Å)	c/a	α(°)	β(°)	γ(°)	$\tilde{a}$(Å)	(meV/atom)	(meV/atom)
					$AlAsSi_3$					
Ordered	17.39	17.37	16.60	0.955	90	90	90.3	5.507	0	0
Al-disordered	17.41	17.40	16.54	**0.951**	90	90	90.1	5.507	+16	+10
Random Alloy	17.40	17.49	16.46	0.944	89.9	90.5	90.2	5.508	+83	+78
					$Al(As_{0.9}N_{0.1})\ Si_3$					
Ordered	17.17	17.18	16.42	0.956	90	90	90.3	5.446	0	0
Al-disordered	17.21	17.21	16.37	**0.952**	90	90	90.1	5.445	+16	+10
Random Alloy	17.26	17.31	16.23	0.939	89.8	90.5	90.5	5.447	+91	+84

Accordingly, there is virtually no molar volume change associated with the orientational disordering.

Several valuable insights are obtained from our simulations. First, we find that orientational disordering of the III-V-IV_3 produces a more cubic average lattice symmetry, since the slightly monoclinic bias[16] induced by the perfect ordering of Al-As bonds is no longer present. Accordingly, the a and b lattice parameters converge, and the c/a ratio tends toward the ideal value for a perfect diamond lattice ($c/a = \sqrt{9/10}$). Note that this regularization of the lattice is manifest both in the model $AlAsSi_3$ system as well as in the $Al(As_{0.9}N_{0.1})Si_3$ counterpart. On this basis, we believe that the rotationally disordered structures reported here are the most representative models of the actual (III-V)IV_3 systems to date. The energetic trends obtained from simulation are also intriguing and indicate that orientational disorder imparts a rather small penalty of only ~15 meV/atom, comparable to the typical energy difference between ordered structures with short-range orientational order, as described in related studies.[15,23] In contrast, simple random distributions of the Al, As, N, and Si constituents lead to a dramatic energy increase due to the occurrence of various III-III and V-V homonuclear bonding arrangements.

Configurational and mixing entropy contributions to the free energy for the partially disordered and random alloy models were also considered. In the latter case, ideal mixing on a tetrahedral lattice containing 20% Al, 20% As, and 60% Si yields a room temperature Gibbs energy contribution $-T\Delta S \sim -2.50$ kJ/mol (5.2 meV/atom for these systems). An upper bound to the configurational entropy for the Al-disordered case (middle panel in Fig. 2) can be obtained by assuming that each tetrahedral Al-As-Si_3 unit can adopt four independent orientations (e.g., 4^N configurations in a crystal containing N units). This yields $\Delta S = Nk_BT$ ln 4 and a corresponding room temperature Gibbs energy contribution $-T\Delta S \sim -3.46$ kJ/mol (7.2 meV/atom). The explicit exclusion of Al-Al bonds can then be accommodated by recognizing that only three of four possible configurations are allowed in the nearest-neighbor unit bonded to the Al-atom vertex of the central unit, while the orientations of the neighboring units bonded to the remaining three vertices are unrestricted. This reduces the possible configurations on a given As-center by a factor of 3/4, yielding $\Delta S = Nk_BT$ ln 3 and Gibbs energy contribution $-T\Delta S \sim -2.74$ kJ/mol (5.7 meV/atom) at room temperature. Based on these considerations, we tabulated the relative free energies for the ordered, Al-disordered, and fully random alloy models in the last column in Fig. 2. The results indicate that the rotationally disordered configurations are only slightly less stable (~10 meV/atom) than the corresponding ordered ground state structures, and that the random alloy configurations are considerably less favorable.

With regard to the structural effects of N incorporation on the group V sites in $AlAsSi_3$, our DFT-LDA simulations predict a reduction in the lattice constant of ~0.06 Å (about 1.1%) for the $Al(As_{0.9}N_{0.1})Si_3$ system, comparable to the observed contraction of the corresponding relaxed lattice constants (~0.05 Å). In addition, a detailed examination of the orientationally disordered $Al(As_{0.9}N_{0.1})Si_3$ equilibrium crystal structures (see Fig. 3) clearly indicates that the lattice distortions around the nitrogen sites are localized within the 1NN and 2NN coordination shells, leaving inherent $AlAsSi_3$-like bond distributions and crystalline order in the intervening regions of the system. These results suggest that it may be feasible to further increase the N content in these systems without adversely affecting the crystalline quality of the epilayer.

III. GROWTH OF $[Al(As_{1-x}N_x)]_ySi_{5-2y}$ ALLOYS

The $[Al(As_{1-x}N_x)]_ySi_{5-2y}$ alloys are grown as epitaxial layers directly on Si(100) substrates using gaseous $N(SiH_3)_3/As(SiH_3)_3$ mixtures and Al atoms in an ultrahigh vacuum (UHV) chamber equipped with standard effusion cells and charged with 99.999% pure aluminum metal. The molecular sources are prepared as colorless volatile liquids possessing significant vapor pressures of ~320 and 10 Torr, respectively, well suited for the gas-source MBE conditions employed in this study. A p-type Si substrate is first sonicated in methanol/isopropanol baths, dipped in a 10% HF/methanol solution, dried in a steam of N_2, and then inserted through the loadlock into the growth chamber at a pressure of $\sim 5\times10^{-8}$ Torr. The wafer is degassed on the sample stage under UHV to remove the surface contaminants until the pressure of the chamber is restored to a base pressure of 10^{-10} Torr. Subsequently, the sample is flashed for 10 seconds at 1150 °C to desorb the native oxide. To commence growth, the substrate is heated to 600–630 °C (the temperature is measured by a

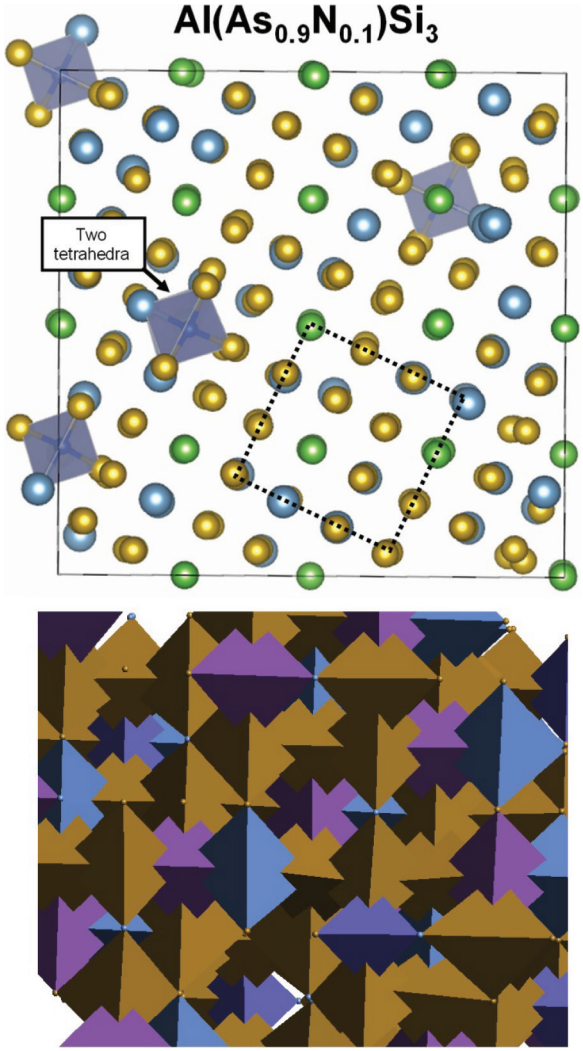

FIG. 3. (Color) (Top) (001) projection of the optimized 240-atom supercell models of $Al(As_{0.9}N_{0.1})Si_3$ indicating that the lattice distortion induced by the N atoms are well localized with intervening regions (dotted box) exhibiting a high degree of crystalline order. The $AlNSi_3$ units are highlighted as shaded polyhedral, while Al, As, and Si atoms are drawn as blue, green, and gold spheres. (Bottom) Polyhedral representation of the above structure including the $AlAsSi_3$, $AlNSi_3$, and $SiSi_4$ tetrahedral units.

single color pyrometer) by passing direct current through it at levels depending on the specific experiment requirements. The temperature is allowed to stabilize for several minutes prior to growth. The precursor mixture is introduced into the chamber at a constant flow controlled by a high precision leak valve, and it is allowed to combine with the Al flux near the substrate surface over the course of the 1–2 hour experiment. The reaction pressure inside the chamber is maintained at 1×10^{-5} Torr during growth via dynamic pumping using a corrosion-resistant turbo pump.

Under the above conditions, films exhibiting a smooth and mirrorlike appearance similar to that of the pristine wafer were produced with thicknesses of 100–200 nm. The corresponding growth rate was varied between 1–2 nm per minute by appropriately adjusting the concentration and flux of the co-reactants and the reaction conditions of the growth process. The samples were initially examined by Nomarski microscopy, which showed a featureless morphology similar to that of the underlying Si. Atomic force microscopy (AFM) images revealed a flat surface with an root mean square (RMS) roughness of 1–2 nm in all cases. We initially pursued the synthesis of stoichiometric $Al(As_{1-x}N_x)Si_3$ alloys with 60% Si and 40% $Al(As_{1-x}N_x)$ via reactions of Al atoms and gaseous mixtures of $N(SiH_3)_3$ with $As(SiH_3)_3$ at low temperatures of 580–600 °C. The growth of the parent $AlAsSi_3$ compound via reactions of $As(SiH_3)_3$ and Al atoms at temperatures above 600 °C produces Si-enriched variants such as $AlAsSi_5$ and $AlAsSi_6$ [here we use the more compact alternative notation $Al(As_{1-x}N_x)Si_{(5-2y)/y}$] arising from the thermal dissociation of $As(SiH_3)_3$. For the $Al(As_{1-x}N_x)Si_3$ alloys, we found that $N(SiH_3)_3$ to $As(SiH_3)_3$ ratios in the range from 2:1 to 4:1 were needed (depending on composition) to be able to substitute any significant N fraction up to a maximum value of $x = 0.10$, as estimated using a combination of Rutherford backscattering (RBS) resonance, secondary ion-mass spectrometry (SIMS), and x-ray diffraction (XRD). The vast excess of $N(SiH_3)_3$ needed in these reactions can be explained by its much lower reaction rate with Al atoms relative to that of $As(SiH_3)_3$, as expected from the diminished nucleophilic strength of the trigonal N over the pyramidal As in the molecular structures.[18]

We note that although the maximum $x \sim 0.10$ N fraction obtained in these experiments is far less than the $x = 0.18$ threshold needed to lattice-match bulk Si, it is nevertheless sufficient to significantly mitigate the strain misfit with the substrate to yield pseudomorphic nitride layers exhibiting single-crystalline structures. RBS experiments at the standard 2 MeV mode were used to obtain concentrations of the heavy Al, Si, and As atoms, while resonance reactions at 3.74 MeV were carried out specifically to probe the minor N content down to levels as low as 2% near the detection limit of 1.5%. For example, the RBS data for a typical 130-nm-thick film with a nominal $AlAsSi_3$ parent-phase composition showed a very weak N signal barely visible above the background, establishing a limiting stoichiometry of $Al(As_{0.90}N_{0.10})Si_3$ where the N fraction of $x = 0.10$ corresponds to an absolute content of 2%. We note that this closely agrees with the indirect determination obtained via XRD in combination with Vegard's Law. In this case the high-resolution XRD (HR-XRD) measurements of the (224) reciprocal space maps and (004) peaks yielded lateral and perpendicular lattice constants of $a = b = 5.4316$ Å and $c = 5.525$ Å, respectively. Using known elastic constants, the relaxed cubic cell parameter was calculated to be $a_0 = 5.480$ Å, which is close to the Vegard's Law estimate of 5.471 Å for the $AlAs_{0.90}N_{0.10}Si_3$ alloy. The RBS and XRD analyses combined constrain the N content of our films to a fairly narrow range of absolute values spanning 2.0–3.5% of the total composition. Finally, a uniform distribution of the N content throughout the layer was obtained from compositional SIMS profiles, which can also be used to estimate relative nitrogen concentrations. For these measurements, the samples were analyzed in negative SIMS mode with a Cs^+ primary beam. The instrument was set to measure the SiN^- molecular ion at a mass to charge ratio of 42, as is commonly done to quantify trace amounts of N in a Si matrix. In all cases, the elemental constituents were found to be homogeneously distributed throughout the film with no

diffusion of elements between substrate and film. The close correspondence between theory and experiment is consistent with substitutional N incorporation within the (III-V)$(IV)_3$ diamondlike structure, in which the Al-As and Al-N pairs are completely isolated from one another and the group As and N atoms are arranged as third-nearest neighbors.

The limited amount of N obtained in the $Al(As_{0.90}N_{0.10})Si_3$ films prompted attempts to enhance the N incorporation by raising the reaction temperature from 600 °C to 625 °C while keeping the precursor ratio fixed at 4:1. In this case, the growth experiments produced $Al(As_{1-x}N_x)Si_5$ alloys that are notably enriched in silicon as measured by RBS and also contain larger amounts of nitrogen relative to As. In this case, the Si enrichment is attributable to the same mechanism involved in the formation of the corresponding $AlAsSi_5$ parent phase. Here the N source does not decompose, and the excess Si is presumably furnished almost exclusively by byproducts of secondary $As(SiH_3)_3$ reaction channels. The temperature-induced N incorporation and simultaneous increase in Si content indicates that the synthesis of $Al(As_{1-x}N_x)Si_5$ is not limited to a fixed Si stoichiometry but represents a general pathway to the formation of alloys with even more broadly tunable properties compared to the $Al(As_{1-x}N_x)Si_3$ system. We found that the resultant epilayers exhibited uniform morphology, flat surfaces, and single-phase structures that grew fully strained to the Si platform, as evidenced by HR-XRD, AFM, and cross-sectional transmission electron microscopy (XTEM).

The RBS plots of the samples revealed strong signals for the constituent Al, Si, and As atoms whose concentration was determined to be close to $AlAs_{1-x}N_xSi_5$ using fits of the 2 MeV spectra, as shown in Fig. 4. These analyses again provided an estimate of $\sim x = 0.08$–0.20 for the bulk N concentration, which is in good agreement with the x levels up to 0.20 ± 0.03 measured by nitrogen resonance depth profiles for several representative samples including $AlAs_{0.80}N_{0.20}Si_5$ and $AlAs_{0.83}N_{0.17}Si_5$. In contrast to the $Al(As_{0.90}N_{0.10})Si_3$, the RBS N peaks of the Si-rich films are sufficiently intense and distinctly resolved to allow standard modeling of the N concentration and establish uncertainties in the fitting

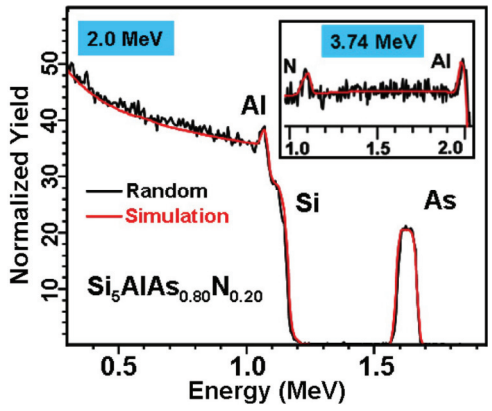

FIG. 4. (Color online) Standard 2 MeV RBS spectrum of an $AlAs_{0.80}N_{0.20}Si_5$ layer grown on Si(100). Inset shows the 3.74 MeV nitrogen resonance plot in which the N signal is clearly resolved. The fits of the data in both cases (red line) give the above composition, which corresponds to an absolute N content of ~3%.

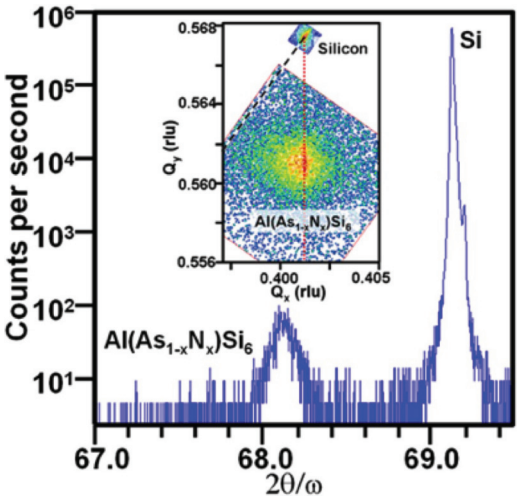

FIG. 5. (Color online) HR-XRD on-axis pilot (blue trace) showing the 004 reflections of the film and substrate. The 224 reciprocal space maps (inset) reveal a perfect vertical alignment of the peak maxima, indicating that the epilayer is compressively strained to the underlying Si.

procedure using the RUMP program.[28] We note that a nominal ±0.03 error in x was estimated by comparing deviations between various fits of the same data. As expected, this error is significant, since the nitrogen represents only a very small fraction (~3%) of the total alloy stoichiometry. In general, we find that the N contents obtained from RBS resonance are also consistent with those obtained indirectly by explicit XRD lattice-constant determinations, supporting the notion that the simultaneous increase of N and Si incorporation into the parent $AlAsSi_3$ structure leads to close lattice-matching with bulk Si. The $Al(As_{0.8}N_{0.2})Si_5$ sample was used as a standard to obtain quantitative N concentrations from the SIMS SiN^- measurements. The analyses resulted in nitrogen contents ranging from 0.5 to 2.9% of the total alloy composition ($x = 0.04$–0.20).

The HR-XRD measurements were also used to corroborate the single-phase character and diamondlike structures of the alloys based on detailed analysis of the on-axis 004 peaks and off-axis 224 reciprocal space maps (see Fig. 5). Using these data for the $AlAs_{0.80}N_{0.20}Si_5$ film, the in-plane lattice parameter is found to be exactly matched to that of the substrate ($a = a_{Si} = 5.430$ Å), while the out-of-plane counterpart is slightly dilated at 5.469 Å due to a residual compressive strain in the epilayer. The corresponding relaxed (a_0) was calculated to be 5.45 Å, compared to the Vegard average of 5.43 ± 0.02 corresponding to $x = 0.20 \pm 0.03$, as determined by RBS resonance.

The XTEM studies (see Fig. 6) reveal uniform layers with flat surfaces and average thicknesses of 95–100 nm, which is comparable to those measured by RBS and ellipsometry. The local microstructure shows sporadic networks of {111}-type stacking defects scattered throughout the middle and upper portions of the epilayer. The origin of these features may be traced back to the intact incorporation of the highly irregular $AlNSi_3$ building blocks furnished by the $N(SiH_3)_3$ precursor, as described in Ref. 18 and Fig. 3. Simulated structural models predict that the tetrahedral $AlNSi_3$ units likely induce

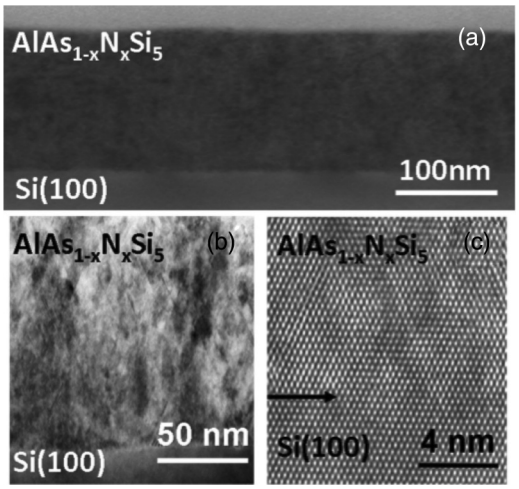

FIG. 6. XTEM micrographs of $Al(As_{0.85}N_{0.17})Si_5$ film grown on Si(100). (a) Image of the entire layer exhibiting a smooth surface and a uniform thickness of ∼100 nm. (b) Enlarged view of the layer revealing a network of {111}-type stacking defects. (c) High resolution image of the interface region showing complete epitaxial registry of the cubic layer with the underlying substrate. We note that occasional Moiré fringe patterns were observed at the interface.

significant steric stress within the parent Si matrix at the atomic scale in contrast to the perfectly normal (regular) $AlAsSi_3$ analogs that are incorporated with minimal deformation of the local structure. The resultant strain can then be relieved via generation of {111}-stacking defects, as observed in Fig. 6(b). The defect levels in our materials are found to diminish as the lattice matching with Si improves with increased Si/N content. This observation provides a conceptual path for the design of low defectivity alloys with lattice dimensions more compatible with that of the Si template via a simultaneous adjustment of the N and Si content.

High-resolution images of the interface show a high degree of epitaxial registry [Fig. 6(c)], as expected due to the close similarity in cell dimensions. Collectively, the XTEM lattice images showed a homogeneous microstructure akin to cubic Si throughout the layer, with no obvious evidence of AlAs or AlN phase segregation. This observation is consistent with the XRD results and further corroborates the phase purity of our materials. The RBS-aligned spectra also suggest structural imperfections presumably due to lattice distortions in the crystal. The spectra (not shown) revealed a significant level of dechanneling toward the film surface due to stacking faults extending from the middle to the upper portion of the layer. In fact, the intensity of the channeled signal in most samples remained essentially unchanged across the entire peak width of the random spectrum from the surface to the interface, as expected from the near uniform spatial distribution of these defects. The ratio of the aligned versus random peak heights (χ_{min}) of the Al, As, and Si signals exhibit values of ∼55% (and higher), which are attributed to the defective upper layer, since XTEM reveals nearly perfect epitaxy at the substrate interface.

We emphasize that increasing the reaction temperatures from 575–625 °C, while maintaining a vast excess of the $N(SiH_3)_3$ co-reactant invariably incorporates a near-stoichiometric amount of nitrogen such that the lattice constants of the target $AlAs_{1-x}N_xSi_5$ systems are very close to the calculated counterparts. Under these process conditions any possible competing reactions producing $AlAs_{1-x}N_x$ impurity phases or amorphous Si-N-H precipitates from the unimolecular decomposition of $N(SiH_3)_3$ are suppressed, facilitating the assembly of crystalline layers as evidenced by our HR-XRD and XTEM characterization. The stabilizing effect of the Si matrix allows a significant substitution of As by N and a precipitous increase in Si content from 60 to 70% without compromising the phase integrity and microstructure quality of the material.

IV. OPTICAL PROPERTIES

The complex dielectric function of our alloy films was measured using a variable angle spectroscopic ellipsometer (VASE; J.A. Woollam Co.) with a computer-controlled compensator. The ellipsometric angles Ψ and Δ were determined at angles of incidence of 65°, 70°, and 75°. The samples are described as a three-layer system consisting of a Si substrate, an $Al(As_{1-x}N_x)_ySi_{5-2y}$ layer, and a surface layer to mimic roughness. The fitted thickness of the surface layer is typically ∼5 nm, consistent with the small value of the RMS surface roughness measured by AFM. The surface layer is modeled as a thin film consisting of a 50% $Al(As_{1-x}N_x)_ySi_{5-2y}$ layer and 50% voids in the Bruggeman approximation. For the dielectric function of the $Al(As_{1-x}N_x)_ySi_{5-2y}$, we find that a combination of two Tauc-Lorentz oscillators[29] provides an excellent fit of the data. It may seem counterintuitive to fit the optical properties of ostensible crystalline films using model functions developed for amorphous materials, but theoretical calculations of the dielectric function of $AlPSi_3$ show that, to a first approximation, the dielectric function of this material can be viewed as a broadened version of that of pure Si.[23] Figure 7 shows the real part ε_1, and Fig. 8 shows the imaginary part ε_2 of the dielectric function obtained for selected samples.

For pure Si, the maximum value of the imaginary part of the dielectric function at room temperature is higher than $\varepsilon_2 = 45$ (Ref. 30). The dielectric function of the films in Fig. 8 has a lower maximum and extended tails into the visible. The overall agreement with the theoretical calculations of Ref. 23 (supporting information) for $AlPSi_3$, both in the lineshape of ε_2 and its magnitude, is quite impressive. The observed low energy tails are important for photovoltaic applications because they lead to a significant enhancement of the optical absorption over the visible range. To quantify the distortion of the dielectric function in the films relative to that of Si, we convolve the Si dielectric function with a Lorentzian. The Lorentzian-broadening Γ is chosen in such a way that the maximum of the broadened Si ε_2 is made equal to the maximum value of ε_2 for the corresponding film. The broadened Si dielectric function is also shown in Fig. 8, and we see that it provides a good, and for some samples an excellent, approximation of the measured dielectric function. In Fig. 9, we show that the optical absorption at 3.0 eV is strongly correlated with the Lorentzian broadening, confirming that Γ is a good parameter to quantify the overall dielectric response of the films. Notice the up-to-five-times higher absorption coefficient of the films relative to that of

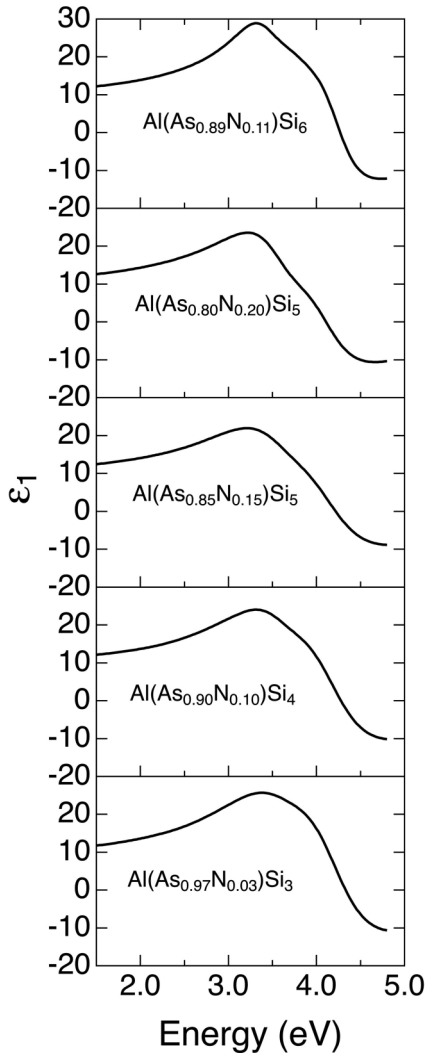

FIG. 7. Real part of the dielectric function of selected $Al(As_{1-x}N_x)Si_{(5-2y)/y}$ films on Si obtained from Tauc-Lorentz fits, as described in the text.

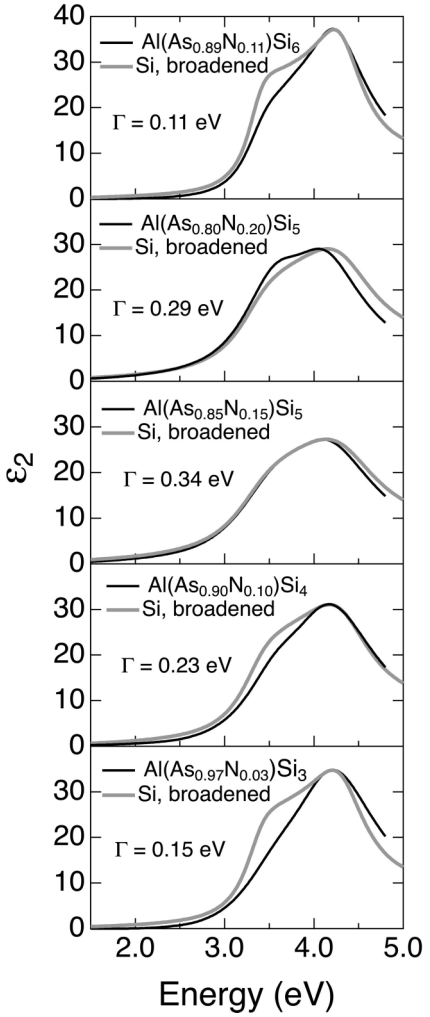

FIG. 8. The solid black lines show the imaginary part of the dielectric function of selected $Al(As_{1-x}N_x)Si_{(5-2y)/y}$ films on Si obtained from Tauc-Lorentz fits, as described in the text. The thick grey lines show the imaginary part of the Si dielectric function broadened to match the maximum value for each film. The Lorentzian broadening parameter used for the Si dielectric function is indicated in each panel.

pure Si. The dependence of Γ on the compositional parameter y and the N concentration x is shown in Fig. 10. There seems to be a trend for an increase in Γ as a function of x, which might be expected in view of the large bond distortions caused by the presence of N substituting As, as seen in Fig. 3. On the other hand, one might also expect the largest broadening for $y = 1$, which corresponds to the highest III-V concentration in the Si matrix. However, this trend is not observed. If anything, the broadening seems to be less for $y = 1$. One intriguing possibility is that $y = 1$ films maintain some residual ordering of the tetrahedral orientations that is not easily detected with Raman spectroscopy[18] but still causes a narrower dielectric function. For $y < 1$, on the other hand, the orientational ordering is completely disrupted by the addition of extra Si atoms, leading to maximum disorder that manifests itself as a broad dielectric function. This interpretation suggests that alloys with $y < 1$ are the best candidates for photovoltaic applications due to their increased visible absorption. As a cautionary note however, we emphasize that this analysis may be too simplistic because films with different values of y were grown at different temperatures; therefore, we cannot completely rule out a different structural origin for the trends observed in Fig. 10.

Sharp optical transitions in solids arise from critical points in the joint density of states. The effect of these critical points on the dielectric function $\varepsilon(E)$ can be easily displayed by computing higher order derivatives $d^n\varepsilon(E)/dE^n$. A fit of these derivatives with model expressions that depend on the character of the critical point gives the strength, width, and energy of the transitions. For this purpose, however, the dielectric function based on Tauc-Lorentz oscillators is not appropriate, because a model function that provides a good fit of $\varepsilon(E)$ does not necessarily give a good fit of its derivatives. Instead, we perform a so-called point-by-point fit in which the layer thicknesses are held fixed at the values determined from the Tauc-Lorentz fits, so that the only remaining adjustable parameters are the real and imaginary part of $\varepsilon(E)$ for the film.[31] A comparison of this point-by-point

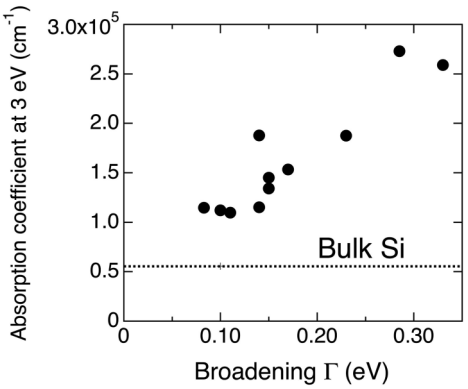

FIG. 9. (Color online) Measured optical absorption at 3.0 eV for the films in Figs. 7 and 8 and several additional $[Al(As_{1-x}N_x)]_ySi_{5-2y}$ samples, plotted as a function of the broadening parameter used to match the imaginary part of the Si dielectric function with that of the film. The horizontal line shows the absorption coefficient of bulk Si at the same photon energy.

$\varepsilon(E)$ with the model functions in Fig. 8 shows an excellent agreement, corroborating the Kramers-Kronig consistency of the point-by-point fits and the general self-consistency of the fit procedure. However, as indicated above, the agreement between the functions does not necessarily translate into an agreement between their derivatives. Accordingly, we only use for our subsequent analysis second-order numerical derivatives of the point-by-point dielectric functions, which are computed using 25 Savitzky-Golay coefficients.[32] These numerical second derivatives are fit with expressions combining terms of the form

$$\frac{d^2\varepsilon}{dE^2} = \frac{Ae^{i\phi}}{(E - E_t + i\Gamma)^{3-i/2}}, \tag{1}$$

where A, E_t, φ, and Γ are the amplitude, transition energy, phase, and broadening, and i is the dimensionality of the critical point ($i = 0$ for excitonic transitions). Results are shown in Fig. 11.

The second derivative of the bulk Si dielectric function over the energy range of Fig. 11 is well characterized by three critical points. The lowest energy one, near 3.32 eV at room temperature, corresponds to the so-called E_0' transition

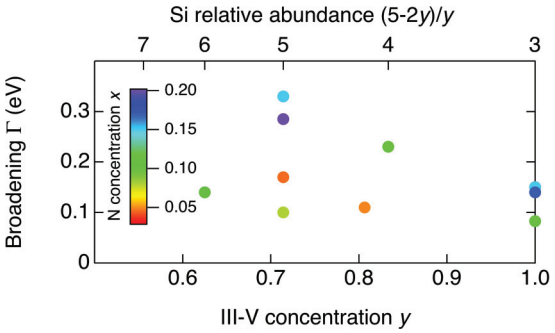

FIG. 10. (Color) The broadening parameter used to match the imaginary part of the Si dielectric function with that of $[Al(As_{1-x}N_x)]_ySi_{5-2y}$ as a function of the III-V concentration y and the N concentration x. The latter dependence is shown using a color scale.

and is best fitted with a two-dimensional (2D) critical point. A second critical point, called the E_1 transition, appears at about 0.1 eV higher and is associated with a much larger joint density of states. This feature is well represented by an excitonic transition.[33] The third critical point corresponds to the maximum of ε_2 in Si and is called the E_2 transition. It is best represented by a 2D critical point. Whereas E_0' and E_1 arise from narrow regions of the Brillouin zone (near the Γ point and along the Γ-L line, respectively), E_2 is a complex combination of contributions from regions near the X point as well as along the Σ line.[33] Above room temperature, E_0' can no longer be distinguished in the ellipsometric spectra, and the dielectric function near 3.3 is well described by a single, broadened E_1 transition. Accordingly, the second derivative of the Si dielectric function at room temperature is reasonably well represented, over the range of Fig. 11, by an excitonic and a 2D critical point. Similar fits, however, give much worse results for the $[Al(As_{1-x}N_x)]_ySi_{5-2y}$ alloys, for which the E_0' critical point must be added to obtain satisfactory agreement with the experimental data. The results of such fits are shown as solid black lines in Fig. 11. The good fit for both the real and imaginary parts provide strong support for the critical point analysis, since the point-by-point fit used to obtain the original ellipsometric data does not impose Kramers-Kronig consistency. The main difference between $[Al(As_{1-x}N_x)]_ySi_{5-2y}$ and Si, in this context, is that the E_1-E_0' separation increases from 0.1 eV in Si to up to 0.66 eV in $[Al(As_{1-x}N_x)]_ySi_{5-2y}$, so that the two transitions can no longer be represented by a single critical point. This is illustrated in Fig. 11, where we show the second derivatives of the Si dielectric function, broadened in such a way that the width of the E_1 transition matches that of the corresponding $[Al(As_{1-x}N_x)]_ySi_{5-2y}$ film. (The broadening values are similar to those in Fig. 8.) We see a close similarity between the two derivatives, except for the additional low energy E_0'-like transition in the films.

As mentioned in the Introduction, theoretical simulations of $AlPSi_3$ and $AlAsSi_3$ indicate the existence of optical transitions at lower energies than those in Si.[17,23] The band structure of an ordered III-VSi_3 compound can be viewed as that of Si folded into the smaller Brillouin zone of the compound and further split and shifted due to the perturbation represented by the III-V atoms. From this perspective, the low-energy transitions in $AlPSi_3$ or $AlAsSi_3$ are seen to originate at the Γ point of the Brillouin zone from precisely the same states that contribute to the E_0' prime transition in pure Si, which are split and shifted in energy by the lower symmetry of the III-VSi_3 compound relative to Si.[17,23] Figure 12 shows side-by-side our calculated band structure of $AlAsSi_3$ for the 10-atom unit cell of its ground structure[17] and the band structure of pure Si for the same supercell. These calculations are performed with the VASP code[24–26] within the LDA;[27] therefore, the absolute energies are underestimated by a significant amount ($\sim$0.7 eV). The energy differences between the two structures in Fig. 12 should, however, be much less affected by the LDA error. The largest downshift of the transition energies derived from E_0' is 0.67 eV in Fig. 12, and the average downshift is 0.34 eV. These are comparable to the observed shifts of the low energy transitions in our $[Al(As_{1-x}N_x)]_ySi_{5-2y}$ films, consistent with our assignment of the lowest feature to E_0'.

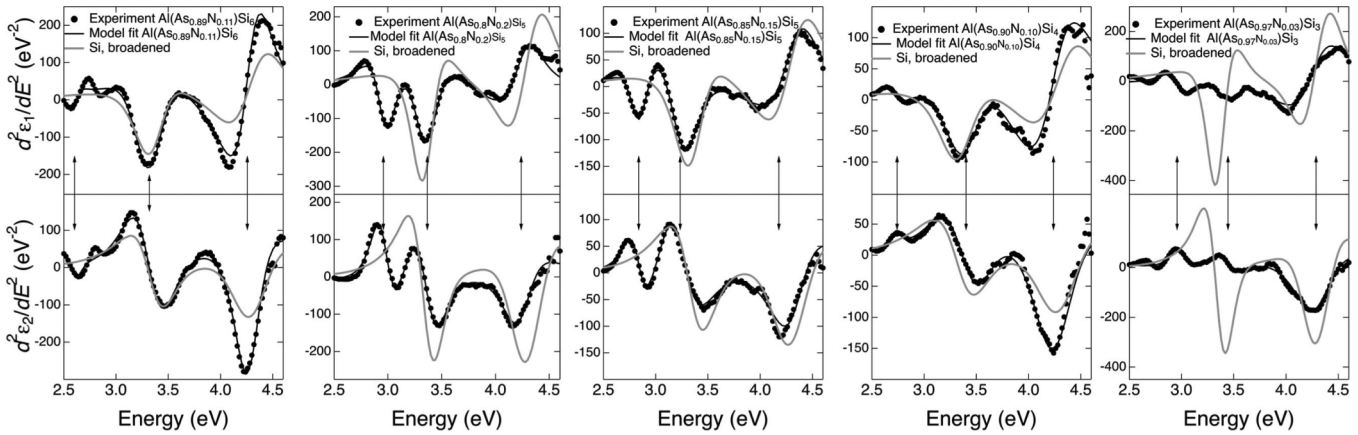

FIG. 11. Circles show numerical second derivatives of the real (top) and imaginary (bottom) dielectric functions of selected $Al(As_{1-x}N_x)Si_{(5-2y)/y}$ films on Si. The solid black lines are fits with Eq. (1) using E_0', E_1, and E_2 critical points, as described in the text. The thick gray lines show to the second derivative of the dielectric function of Si, broadened to match the width of the E_1 transition in the alloy films. The vertical arrows mark the energies of the three transitions obtained from the fits.

Since the splittings due to the lower symmetry are present even in stoichiometric $AlAsSi_3$ compounds, the additional disorder induced by the incorporation of nitrogen for $x > 0$ and extra Si atoms for $y < 1$ can only induce some inhomogeneous shifts of the state energies, which manifest themselves as an increased broadening and lead to observation of a single rather than several optical transitions in this energy range. It can also be speculated that this additional disorder increases the downshift of the E_0'-like transitions due to additional level-repulsion channels, making them easier to observe due to the increased separation with the E_1 transitions.

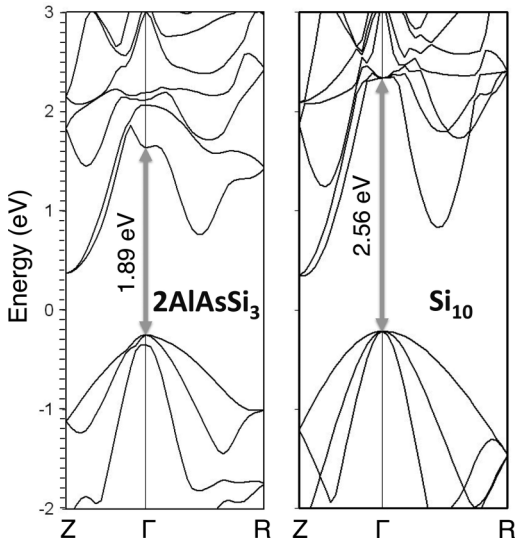

FIG. 12. Comparison of the band structures of $AlAsSi_3$ and Si in a 10-atom unit cell structure, as described in Ref. 17. The arrows indicate the lowest energy direct transitions at the center of the Brillouin zone, which in the case of Si correspond to the so-called E_0' transition between p-bonding and p-antibonding states (the spin-orbit interaction is not included in the calculation). The experimental value of E_0' in Si is 3.32 eV. The discrepancy is a well-known shortcoming of the local density approximation, but calculated relative trends are usually much more accurate.

The energies of the measured transitions are given in Table II. The values quoted have been corrected for the residual epitaxial strain using deformation potential theory. Since the strains are relatively small and we are unable to resolve any strain-related splitting, it is reasonable to use only the hydrostatic component of the strain for the corrections. For the E_1 and E_2 transitions, we write the strain shifts as

$$\delta E = \sqrt{3} D_{11}(2\varepsilon_{\parallel} + \varepsilon_{\perp}), \tag{2}$$

where $\varepsilon_{\parallel}$ and $\varepsilon_{\perp}$ are the components of the strain in the growth plan and in the growth direction, respectively. Obviously, no deformation potentials are available in the literature for III-VSi_3 compunds, so we use Si values. The deformation potential D_{11} is taken as $D_{11} = -9.72$ eV (E_1 gap) and $D_{11} = 2.6$ eV (E_2 gap) (Ref. 34). For the E_0' gap, the only study of the strain dependence of the transition energy appears to be the work of Munguía and coworkers.[35] If we assume that their measured shifts are given by an expression of the form

$$\delta E = D(2\varepsilon_{\parallel} + \varepsilon_{\perp}), \tag{3}$$

we obtain $D = -7.8$ eV from fitting these data. It is difficult to extract clear compositional dependence trends from the data in Table II, particularly because the compositional dependence space is 2D in x and y, combined with the aforementioned difference in the growth conditions as a function of y.

TABLE II. Critical point energies for selected $Al(As_{1-x}N_x)Si_{(5-2y)/y}$ samples obtained from the fits in Fig. 10 corrected for strain shifts as discussed in the text. Typical errors in the fit energy values are in the 0.01 eV range.

	E_0' (eV)	E_1 (eV)	E_2 (eV)
$AlAs_{0.97}N_{0.03}Si_3$	2.90	3.29	4.33
$AlAs_{0.90}N_{0.10}Si_3$	3.02	3.21	4.11
$AlAs_{0.85}N_{0.15}Si_3$	2.98	3.16	4.51
$AlAs_{0.90}N_{0.10}Si_4$	2.66	3.24	4.29
$AlAs_{0.85}N_{0.15}Si_5$	2.78	3.12	4.20
$AlAs_{0.80}N_{0.20}Si_5$	2.92	3.27	4.27
$AlAs_{0.86}N_{0.11}Si_6$	2.54	3.20	4.31

V. CONCLUSIONS

In this work, we have presented an explicit model of disorder in compounds of the form III-V-Si_3 that is compatible with our proposed growth mechanism via incorporation of entire III-IV-Si_3 tetrahedral units into the growing film. The calculated disordered alloys have energies that are marginally above the ground state ordered lattices; therefore, they are highly likely to be the dominant structural form of grown films, explaining their broadened Raman spectra. The optical studies show that distinct absorption transitions calculated for the ordered ground-state structures are still observable in the disordered phases, demonstrating that such transitions are robust against orientational disorder.

For applications in photovoltaics, compounds with increased optical absorption in the visible are desired. This work suggests that Si-rich $[Al(As_{1-x}N_x)]_ySi_{5-2y}$ alloys with $y \sim 0.7$ are optimal for this application due to their maximally broadened dielectric function with respect to Si, with tails in the imaginary part that extend into the visible, enhancing the absorption by one order of magnitude. The narrower dielectric function observed for $y = 1$ suggests that these compounds may have some residual ordering that does not manifest itself in the Raman spectra but influences on the optical properties.

ACKNOWLEDGMENTS

We thank Mr. Tylan Watkins for help growing some of the samples used in this study (Ref. 18), for subsequent analysis and characterization, and Prof. Stefan Zollner (New Mexico State University) for suggesting the Tauc-Lorentz fits for III-V-Si_3 alloys. This work was partially funded by Grant No. DMR-0907600 from the National Science Foundation.

[1] K. E. Newman and J. D. Dow, Phys. Rev. B **27**, 7495 (1983).
[2] H. Holloway and L. C. Davis, Phys. Rev. Lett. **53**, 1510 (1984).
[3] K. Kim and E. A. Stern, Phys. Rev. B **32**, 1019 (1985).
[4] L. C. Davis and H. Holloway, Phys. Rev. B **35**, 2767 (1987).
[5] L. C. Davis and H. Holloway, Phys. Rev. B **38**, 4294 (1988).
[6] R. Osório, S. Froyen, and A. Zunger, Phys. Rev. B **43**, 14055 (1991).
[7] B. Salazar-Hernández, M. A. Vidal, M. E. Constantino, and H. Navarro-Contreras, Solid State Commun. **109**, 295 (1999).
[8] G. Giorgi, M. Schilfgaarde, A. Korkin, and K. Yamashita, Nanoscale Research Letters **5**, 469 (2010).
[9] R. J. Baird, H. Holloway, M. A. Tamor, M. D. Hurley, and W. C. Vassell, J. Appl. Phys. **69**, 226 (1991).
[10] A. G. Norman, J. M. Olson, J. F. Geisz, H. R. Moutinho, A. Mason, M. M. Al-Jassim, and S. M. Vernon, Appl. Phys. Lett. **74**, 1382 (1999).
[11] D. J. Friedman, S. R. Kurtz, and J. F. Geisz, in *Proceedings of the Twenty-Ninth IEEE Photovoltaic Specialists Conference* (IEEE, Piscataway, NJ, USA, 2002), p. 856.
[12] K. C. Cadien, A. H. Eltoukhy, and J. E. Greene, Appl. Phys. Lett. **38**, 773 (1981).
[13] T. N. Krabach, N. Wada, M. V. Klein, K. C. Cadien, and J. E. Greene, Solid State Commun. **45**, 895 (1983).
[14] I. Banerjee, D. W. Chung, and H. Kroemer, Appl. Phys. Lett. **46**, 494 (1985).
[15] T. Watkins, A. V. Chizmeshya, L. Jiang, D. J. Smith, R. T. Beeler, G. Grzybowski, C. D. Poweleit, J. Menendez, and J. Kouvetakis, J. Am. Chem. Soc. **133**, 16212 (2011).
[16] T. Watkins, L. Jiang, C. Xu, A. V. G. Chizmeshya, D. J. Smith, J. Menéndez, and J. Kouvetakis, Appl. Phys. Lett. **100**, 022101 (2012).
[17] G. Grzybowski, T. Watkins, R. T. Beeler, L. Jiang, D. J. Smith, A. V. G. Chizmeshya, J. Kouvetakis, and J. Menéndez, Chem. Mater. **24**, 2347 (2012).
[18] J. Kouvetakis, A. V. G. Chizmeshya, L. Jiang, T. Watkins, G. Grzybowski, R. T. Beeler, C. Poweleit, and J. Menéndez, Chem. Mater. **24**, 3219 (2012).
[19] P. Lautenschlager, P. B. Allen, and M. Cardona, Phys. Rev. B **31**, 2163 (1985).
[20] G. Samsonidze, M. L. Cohen, and S. G. Louie, Phys. Rev. B **84**, 195201 (2011).
[21] J. F. Geisz, J. M. Olson, D. J. Friedman, K. M. Jones, R. C. Reedy, and M. J. Romero, *Conference Record of the Thirty-first IEEE Photovoltaic Specialists Conference, 2005* (IEEE, Piscataway, 2005), pp. 695–698.
[22] D. Munteanu and J. L. Autran, J. Non-Cryst. Solids **357**, 1884 (2011).
[23] J. H. Yang, Y. Zhai, H. Liu, H. Xiang, X. Gong, and S. H. Wei, J. Am. Chem. Soc. **134**, 12653 (2012).
[24] G. Kresse and J. Hafner, Phys. Rev. B **47**, 558 (1993).
[25] G. Kresse and J. Furthmüller, Comput. Mater. Sci. **6**, 15 (1996).
[26] G. Kresse and J. Furthmüller, Phys. Rev. B **54**, 11169 (1996).
[27] D. M. Ceperley and B. J. Alder, Phys. Rev. Lett. **45**, 566 (1980).
[28] L. R. Doolittle, Nucl. Instrum. Methods Phys. Res., Sect. B **9**, 344 (1985).
[29] G. E. Jellison, Jr., and F. A. Modine, Appl. Phys. Lett. **69**, 371 (1996).
[30] D. E. Aspnes and A. A. Studna, Phys. Rev. B **27**, 985 (1983).
[31] V. R. D'Costa, C. S. Cook, A. G. Birdwell, C. L. Littler, M. Canonico, S. Zollner, J. Kouvetakis, and J. Menendez, Phys. Rev. B **73**, 125207 (2006).
[32] J. Steiner, Y. Termonia, and J. Deltour, Anal. Chem. **44**, 1906 (1972).
[33] P. Lautenschlager, M. Garriga, L. Vina, and M. Cardona, Phys. Rev. B **36**, 4821 (1987).
[34] P. Etchegoin, J. Kircher, and M. Cardona, Phys. Rev. B **47**, 10292 (1993).
[35] J. Munguía, J. M. Bluet, H. Chouaib, G. Bremond, M. Mermoux, and C. Bru-Chevallier, J. Phys. D **43**, 255401 (2010).